Modelling of Stellar Atmospheres
IAU Symposium, Vol. xxx, xxxx
N. E. Piskunov, W. W. Weiss, D. F. Gray, eds.

Effects of domain size on surface simulations of the sun.

F. J. Robinson, L. H. Li, P. Demarque, S. Sofia

Astronomy Department, Yale University, New Haven, CT, USA

Y.-C. Kim

Astronomy Department, Yonsei University, Seoul, South Korea

D. B. Guenther

St Mary's University, Halifax, N.S., Canada

Abstract.

We report on a set of realistic 3D simulations of the upper radiation/convection transition region in the Sun. Our approach is to solve the conservation form of the Navier Stokes equations in a strictly conserved domain (closed box). Radiative transport in the highly superadiabatic layer (SAL) is dealt with by solving the 3D Eddington Approximation (Unno & Spiegel 1966).

If the box is too shallow, when the strong downdrafts hit the bottom boundary, the overall flow was speeded up. The fast flowing fluid was overly convectively efficient and this resulted in a lowering of the SAL peak. Using the Li et al (2002) parameterisation of turbulence, the computed p-mode frequencies are too high (up to 40 μ Hz greater than the observed frequencies) if the box is too shallow, but show a significant improvement over the standard stellar model (within 5 μ Hz of observed frequencies), if a bigger box is used. If the box width is too small to accommodate at least two granules, then in the shallower regions the turbulent energy is underestimated.

We also present preliminary results of 3D simulations of the Sun at later stages of evolution. It seems that the diameter of the granules in the turn-off star are smaller than in the present Sun. This may be due to the smaller convection zone.

1. Introduction

It is now possible to perform physically realistic 3D simulations of the surface layers of the Sun which take into account the complex interaction between radiative and convective energy transports (Stein & Nordlund 1998 and references therein; Kim & Chan 1998; hereafter denoted SN and KC). With the exception of KC, most realistic solar convection models (i.e. simulations which include a realistic equation of state, realistic opacities and proper treatment of radiative transfer in the shallow layers) have been done using the highly successful SN model (e.g. Rosenthal et al. 1999, Asplund et al. 2000). More ambitious methods, use adaptive meshes (Fryxell et al 2000). or attempt to extend simulations in to the middle chromosphere (Wedemeyer et al 2001).

The motivation of this poster is to apply the model developed by Kim & Chan (1998) to different sized domains and to other stars. In particular we examine how the domain size effects the simulation results and subsequently explore surface convection in the Sun as it evolves to the turn-off and the subgiant.

The poster paper is set out as follows. Firstly we explain the model and the numerical techniques, then present the main results. This is followed by some simulations of convection in the Sun at later evolutionary stages and finally we present our conclusions.

2. Modelling realistic solar surface convection

To model realistic surface layer convection in the Sun we take the following approach:

1. Using a standard stellar model (YREC e.g. see Guenther et al. (1992)), we compute the initial density ρ and internal energy e for the 3D simulations. From a random velocity field, we then compute 5 dependent conservative variables, ρ, $E(= 1/2\rho v^2 + e)$, ρv_x, ρv_y and ρv_z.

2. Using tables of the OPAL equation of state and the OPAL opacities we compute $P(\rho, e), T(\rho, e), \kappa(\rho, e)$, $c_{\rm p}(\rho, e)$, $\nabla_{\rm ad}(\rho, e)$ and some thermodynamic derivatives.

3. The radiation flux is then computed using the diffusion approximation in the optically thick regions and the 3D Eddington approximation in the optically thin layers.

4. We then integrate the Navier Stokes equations over one time step to compute a new set of dependent variables and return to (2).

2.1. Realistic physics: steps 1 and 2

The solar model uses the same physics as described in Guenther & Demarque (1997). In particular, the low temperature opacities of Alexander & Ferguson (1994) and the OPAL opacities and equation of state were used (Iglesias & Rogers 1996). Hydrogen and helium ionisation, and the diffusion of both helium and heavy elements are included. This provides the initial stratification.

For each timestep of the numerical integration we need to solve the complex equation of state (step 2). This adds considerable computational time compared to an ideal simulation (e.g. with a perfect gas). The 3D hydrodynamical simulations use identical opacities and equation of state as used in the 1D reference model. The side boundaries are periodic, while the top and bottom boundaries are stress free. A constant heat flux flows through the base, and the top is a perfect conductor. To ensure that mass, momentum and energy are fully conserved, we use impenetrable (closed) top and bottom boundaries.

A particular model is specified by g (the effective gravity at the surface) and $T_{\rm eff}$ (the effective temperature at the surface). $T_{\rm eff}$ enters the energy equation via the flux term f at the base. Aside from the viscosity coefficients there are no other free parameters.

2.2. Radiation transfer: step 3

In the SAL region, the photon mean free path is not small enough to use the diffusion approximation. The alternatives are to either solve the full radiative transport equation for a few rays (SN) or to apply the 3D Eddington approximation (KC). If enough rays are used, then solving the full equation would be more accurate than the Eddington approximation. However, doing the ray transfer is also computationally expensive. In the frequency-dependent case (4 frequencies), about 50% of the CPU time is used for the radiative transfer part (private communication with H.-G. Ludwig).

In this paper, we have treated radiative transfer in the same way as KC. In the deeper part of the domain ($\tau > 10^4$), we used the diffusion approximation,

$$Q_{\rm rad} = \nabla \cdot \left[\frac{4acT^3}{3\kappa\rho} \nabla T \right] , \tag{1}$$

where κ is the Rosseland mean opacity, a is the Boltzmann constant and c is the speed of light. In the shallow region, the photon mean free path is at least one tenth of the depth of the atmosphere, so the diffusion approximation may not apply. Instead $Q_{\rm rad}$ is computed as

$$Q_{\rm rad} = 4\kappa\rho(J - B) \tag{2}$$

where mean intensity J is computed by using the generalized three-dimensional Eddington approximation (Unno & Spiegel 1966), and B is the Planck function,

$$\nabla \cdot \left(\frac{1}{3\kappa\rho} \nabla J \right) - \kappa\rho J + \kappa\rho B = 0. \tag{3}$$

This formulation is exact for isotropic radiation in a gray atmosphere, and without requiring local thermodynamic equilibrium, the Eddington approximation describes the optically thick and thin regions exactly. To study spectral line profiles and spectral energy distribution, requires frequency dependent radiative transfer. However, in a study of the SAL and comparison with results of helioseismology, a gray atmosphere is found to be adequate.

2.3. Hydrodynamics: step 4

For deep ($v << c_{\rm s}$) and efficient ($\nabla - \nabla_{\rm ad}$ just above zero) convection, Chan & Sofia (1989) showed that MLT is a very good approximation to the real situation. However, in the SAL, both the Mach number $(v/c_{\rm s})^2$ (v is the flow velocity and $c_{\rm s}$ is the sound speed), and the superadiabaticity $\nabla - \nabla_{\rm ad}$, can be of order unity. In this case, MLT is unlikely to apply. The validity of this argument is confirmed by the run of sound speed in the SAL derived by inversion of the helioseismic data, which disagrees with the MLT model (Basu & Antia 1997).

In such an environment, the governing hydrodynamic equations are the fully compressible Navier-Stokes equations (see e.g. Kim et al. 1995).

$$\begin{aligned}
\partial\rho/\partial t &= -\nabla\cdot\rho\mathbf{v} && (4)\\
\partial\rho\mathbf{v}/\partial t &= -\nabla\cdot\rho\mathbf{v}\mathbf{v} - \nabla P + \nabla\cdot\mathbf{\Sigma} + \rho\mathbf{g} && (5)\\
\partial E/\partial t &= -\nabla\cdot[(E+P)\mathbf{v} - \mathbf{v}\cdot\mathbf{\Sigma} + \mathbf{f}] && (6)\\
&\quad +\rho\mathbf{v}\cdot\mathbf{g} + Q_{\mathrm{rad}}
\end{aligned}$$

where $E = e + \rho v^2/2$ is the total energy density and $\rho, \mathbf{v}, P, e$ and $\mathbf{g}$, are the density, velocity, pressure, specific internal energy and acceleration due to gravity, respectively. Q_{rad} is the energy transferred by radiation. Ignoring the coefficient of bulk viscosity, the viscous stress tensor for a Newtonian fluid is $\Sigma_{ij} = \mu(\partial v_i/\partial x_j + \partial v_j/\partial x_i) - 2\mu/3(\nabla\cdot\mathbf{v})\delta_{ij}$.

In fully developed turbulence the ratio of the length of the largest eddy to the dissipation length is $\mathrm{Re}^{3/4}$, where Re is the Reynolds number (Landau & Lifshitz 1987). In the Sun, Re is the order of 10^{12} which means there are about 10^9 scales per dimension. A 3D direct numerical simulation (DNS) of the sun would thus require about 10^{27} grid points !

The Large Eddy simulation (LES) approach assumes that the small scales are independent of the resolved scales (large eddies) and can be parameterised as a diffusion process. In this case the viscosity μ is an eddy viscosity is defined in terms of the resolved velocity shear (Smagorinsky 1963),

$$\mu = \rho(c_\mu\Delta)^2(2\boldsymbol{\sigma}:\boldsymbol{\sigma})^{1/2}. \tag{7}$$

The colon inside the brackets denotes tensor contraction of the rate of strain tensor $\sigma_{ij} = (\nabla_i v_j + \nabla_j v_i)/2$. The SGS eddy coefficient c_μ, is set to 0.2, the value for incompressible turbulence, and $\Delta = (\Delta_x\Delta_y)^{1/2}\Delta_z$ is an estimate of the local mesh size. To handle shocks, μ is multiplied by $1 + C\cdot(\nabla\cdot\mathbf{v})^2$, where the constant C is made as small as possible, while maintaining numerical stability. As μ is dependent on the velocity divergence, any large velocity gradients are smoothed out by the increased viscosity. If a shock occurs it is not resolved, but smeared out by this local increase in viscosity.

The diffusive flux $\mathbf{f} = -(\mu/\mathrm{Pr})T\nabla S$, where the horizontal mean of $\nabla S \leq 0$ i.e. the convection zone, and $\mathbf{f} = -(\mu c_{\mathrm{p}}/\mathrm{Pr})\nabla T$ where the horizontal mean of $\nabla S \geq 0$ i.e. the radiation zone. In the convection layer the SGS diffusive flux tends to smooth out entropy fluctuations and make the layer close to adiabatic (in analogy with turbulent mixing). The change in the form of the diffusive flux above the convection boundary is necessary because the SGS's should continue to transport heat radially outwards though the top of the box. Away from the horizontal boundaries, $\mathbf{f}$ is close to zero. The Prandtl number $\mathrm{Pr} = \nu/\kappa$ (ν is the kinematic viscosity and κ is the thermal diffusivity) is 1/3. Due the inclusion of radiative energy transport (see section below), the effective Pr is actually much smaller and not constant.

3. Numerical methods

The simulation domain is a small box of aspect ratio 1.5, which includes the photosphere and top part of convection zone. Using a code developed by Chan

& Wolff (1982), an implicit scheme (the Alternating Direction Implicit Method on a Staggered grid or ADISM) relaxes the fluid to a self consistent thermal equilibrium. The advantage of ADISM is that it allows us to use a large time step while still include sound waves. The layer is fully relaxed if; the energy flux leaving the top of the box is within 5 % of the input flux at the base: the horizontally averaged vertical mass flux is less than 0.001 at every vertical level; and the overall thermal structure, i.e. the run of $\nabla - \nabla_{\rm ad}$ (or Log T versus Log P), does not change over time. These three criteria must be satisfied, before any useful statistical data can be gathered. The relaxation typically takes about 5 hours of solar surface convection time. A second order explicit method (Adams-Bashforth time integration) gathers the statistics of the time averaged state. The statistical integration time is about 2500 seconds of solar surface convection, and requires about half a million time steps. On an 667 MHz Alpha processor, each integration step on a $80 \times 80 \times 80$ grid, requires about 5 seconds of CPU time. A full simulation on a fine grid (120^3) with a domain depth of 2.5 Mm, takes about 3 months to run.

4. Results

4.1. Effect of domain size

After substantial numerical testing which is described in appendix 1, we found two important results:

1. An undesirable effect of the impenetrable horizontal boundary at the bottom is too speed up the overall flow. In a faster flow convection carries more of the total flux thus enhancing convective efficiency throughout the box. This means radiation carries less energy and near the surface $\nabla - \nabla_{\rm ad}$ is artificially small. To avoid this numerical artifact, the boundary has to be positioned far enough away from the surface, so that the velocity at the base is small and uncorrelated from the motions near the surface.

2. If the width of the domain is too small then the turbulent kinetic energy in the granules is too small. This is because the largest granules cannot exist in a narrow box. This is an important consideration in the surface region, but less crucial lower down where the diameter of convective cells are smaller than the width of the box. To remove this numerical artifact the aspect ratio is increased until two or more granules can be seen in the surface layers.

4.2. Comparison with previously published work

After minimising the effects of (1) and (2), the velocities and thermal structures became close to those found in simulations by previous investigators. As an example, we show the rms vertical velocity (figure 1 (a)) and the superadiabaticity (figure 1 (b)). Away from the top and bottom boundaries the plots compare favorably with Figure 3 (rms velocity) in Asplund et al and Figure 3 ($\nabla - \nabla_{\rm ad}$) in Rosenthal et al. The most noticeable differences occur at the top and bottom because in our simulations the vertical velocity drops to zero there. In Asplund

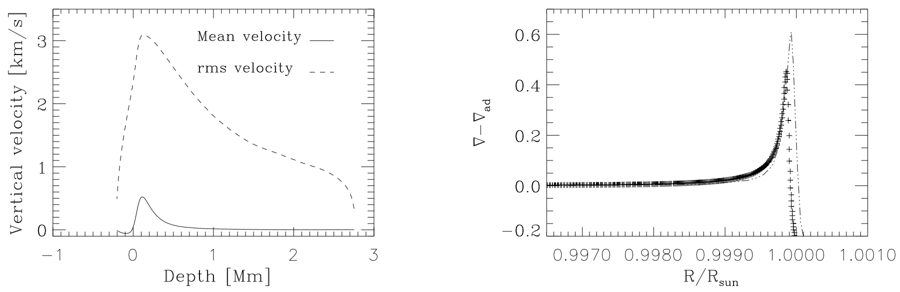

Figure 1. The left plot contains the rms and mean vertical velocity from a 3D simulation. The right plot is $\nabla - \nabla_{\rm ad}$ from a standard solar model (pluses) and the corresponding 3D simulation (triple-dot-dashes). Away from the boundaries the 3D simulations compare favorably with previously published results.

et al. the transmitting boundaries allows the velocity to decrease more naturally.

5. Implementation of 3D turbulence into 1D stellar models

The turbulent velocity is defined by the velocity variance,

$$v = \left[\sum_{i=1}^{3}(\overline{V_i^2} - \overline{V_i}^2)\right]^{1/2}, \tag{8}$$

where the overbar denotes horizontal and temporal averaging of a 3D hydrodynamical simulation.

By analogy with the work of Lydon & Sofia (1995) on magnetic effects, the 3D turbulence is parameterized in terms of two quantities, the turbulent kinetic energy per unit mass (Li et al. 2002),

$$\chi = \frac{1}{2}v^2 \tag{9}$$

and an anisotropy parameter,

$$\gamma = 1 + 2(v_z/v)^2. \tag{10}$$

The z direction is parallel to the radial direction. As the 3D simulations are in a small box , curvature effects are ignored, hence $v^2 = {v_x}^2 + {v_y}^2 + {v_z}^2$.

In an ideal gas $\gamma = c_{\rm p}/c_{\rm v}$, the internal energy $E = c_{\rm v}T/\mu$ and $P = \rho RT/\mu$ (μ is the mean molecular weight), so that

$$\gamma = 1 + P/(\rho E) \tag{11}$$

If we replace P by $P_{\rm turb}(= \rho {v_z}^2)$ and E by χ then we get:

$$P_{\rm turb} = (\gamma - 1)\rho\chi. \tag{12}$$

The equation of state becomes,

$$\rho = \rho(P_T, T, \chi, \gamma)$$

where $P_T = P_{\rm gas} + P_{\rm rad} + P_{\rm turb}$.
The continuity equation and the equation of transport of energy by radiation remain the same regardless of turbulence. In terms of γ and χ the hydrostatic equilibrium is,

$$\frac{\partial P_T}{\partial M_r} = -\frac{GM_r}{4\pi r^4} - \frac{2(\gamma-1)\chi}{4\pi r^3}. \tag{13}$$

The energy conservation equation is also affected by the inclusion of turbulent kinetic energy χ

$$\frac{\partial L_r}{\partial M_r} = \epsilon - T\frac{dS}{dt} \tag{14}$$

where

$$TdS = dU + (P_T - P_{\rm turb})d(1/\rho) + d\chi \tag{15}$$

The convective flux $F_{\rm conv} = \rho TdS\, V_{\rm conv}$ now includes the turbulent kinetic energy flux $\chi V_{\rm conv}$ (without turbulence $\chi = 0$, so $d\chi = \chi$). Equation 15 is the 'non-standard form' of the 2nd law as described in Lydon & Sofia. As turbulence is in general anisotropic it is wrong to treat the work done by turbulence as $-P_{\rm turb}dV$. This is essentially because $P_{\rm turb}$ is a tensor and $P_{\rm gas}$ is a scalar.

The equation of energy transport by convection, does not change in form, but ∇ is different from that without turbulence. The equations that govern envelope integrations are changed accordingly.

5.1. Solar p-mode oscillation frequencies

The runs of χ and γ for a model in which the lower boundary is too close to the SAL and a much deeper model can be incorporated into the 1D stellar model using the Li et al method. For each run, the *p*-mode frequencies for $l = 0, 1, 2, 3, 4, 10...100$, are computed using Guenther's pulsation code, (1994). under the adiabatic approximation. When comparing the computed and observed eigenfrequencies, one should really include the proper modeling of radiative gains and losses by computing the non-adiabatic frequencies (Guenther 1994). However, to help isolate the effects of turbulence on the *p*-mode frequencies, we computed the adiabatic frequencies. The difference between observed and computed adiabatic *p*-mode frequencies for the standard solar model is shown in figure 2. The frequency difference is scaled by the mode mass Q_{nl} (e.g., Christensen-Dalsgaard & Berthomieu 1991). With the Q_{nl} weighting in place, the mismatch between the observed and computed adiabatic frequencies is clear, the mismatch increases as the frequency increases, thus pointing to a problem in the surface layers. Without the Q_{nl} weighting the mismatch would appear to varying degree at all frequencies and therefore it would not be as easy to claim that the outer layers are responsible for the mismatch.

In the statistically steady state (after the flow is thermally relaxed), the turbulent kinetic energy flux should be proportional to the energy input rate at the base f_b. However, if the box is too shallow or the width is too narrow, then due too the numerical effects summarised in 4.1., the turbulent kinetic energy χ can be wrong. In such a simulation, the computed adiabatic frequencies

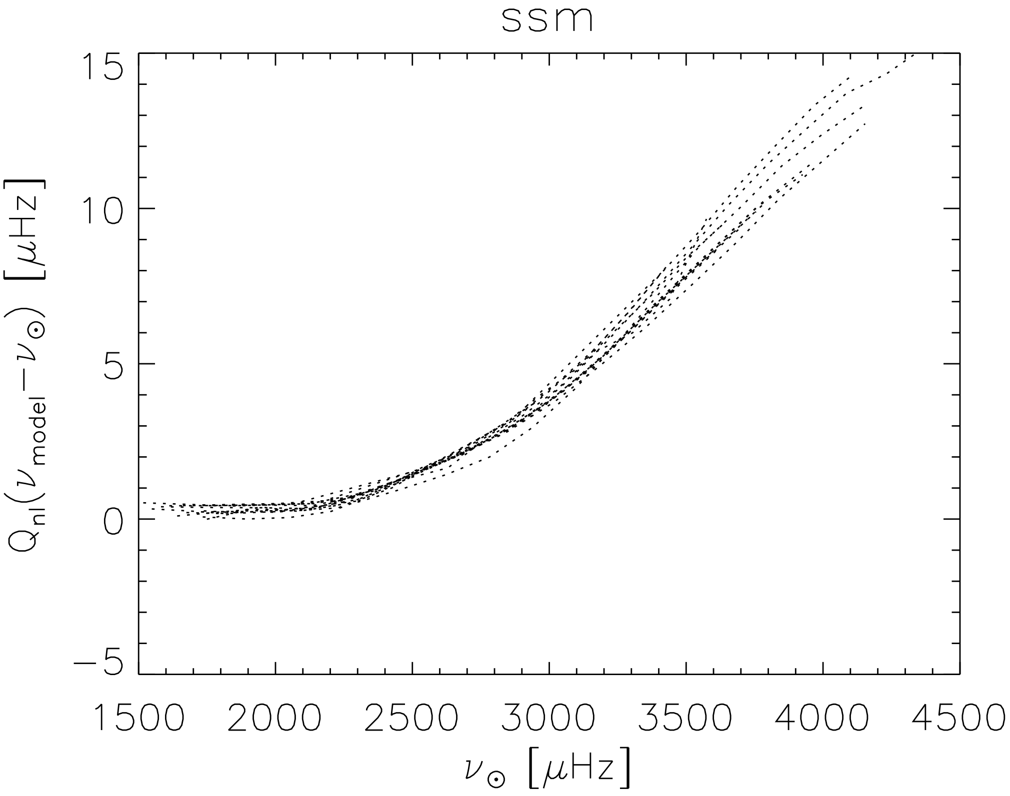

Figure 2. The difference between observed and computed p- mode frequencies for Standard Solar model (see text).

with turbulence included, are much worse than the standard solar model, figure 3 (a). However, if the box is big enough then the derived frequencies are improved considerably (figure 3 (b)). The difference between computed and observed frequencies are now less than 5 μ Hz. The substantial improvement in the eigenfrequencies by including the turbulent kinetic energy, reflects the non-local nature of convective turbulence. The assumption that production equals dissipation is not true. Chan & Sofia (1989) showed that the dissipation of kinetic energy is non-local. A significant amount of kinetic energy is carried away from the production region and is dissipated at the upper and lower boundaries.

The inclusion of turbulent kinetic energy in 1D models in addition to turbulent pressure, has a similar effect on the adiabatic frequencies to the inclusion of radiative losses/gains (computation of non-adiabatic frequencies). Both reduce the difference between the adiabatic frequencies and the observed frequencies by an order of magnitude. This mean that the turbulent correction to the p-modes are as important as radiative gains/losses.

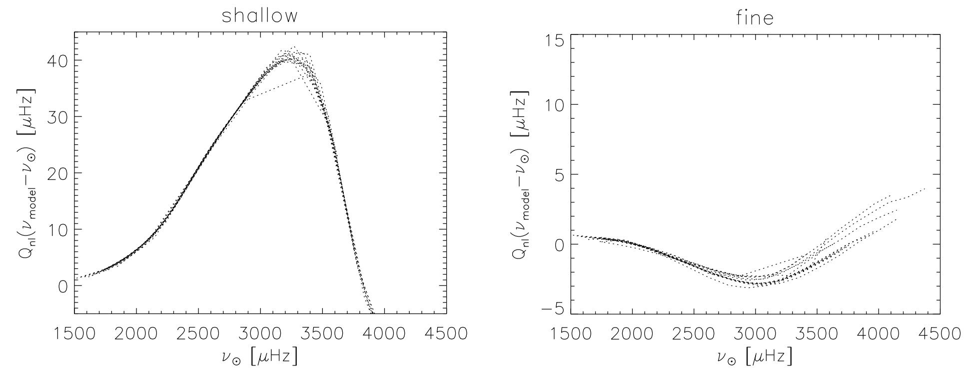

Figure 3. The difference between observed and computed p- mode frequencies with turbulence included from a shallow 3D convection simulation (figure (a)) and a much deeper simulation (figure (b)).

6. Granulation in the Sun, Turn-off and sub-giant stars.

Using the same techniques that we applied to the Sun, we evolved a stellar model of one solar mass beyond the age of the present Sun, to the main sequence turn-off and sub-giant stages and completed 3D simulations for each case.

Preliminary results indicate that the characteristics of the granules seem to change with age (i.e. as the star evolves along the $logg - logT_{\rm eff}$ plane). From top to bottom of each column in figure 4, are the horizontal contours plots of vertical velocity, located at the surface (where $\nabla - \nabla_{\rm ad}$=0), the peak of the SAL (where $\nabla - \nabla_{\rm ad} = |\nabla - \nabla_{\rm ad}|_{\rm max}$), the base of the SAL (where the slope of $\nabla - \nabla_{\rm ad}$ first becomes small) and at a point in the deeper layers. The first, second and third columns are from models of the Sun (4×4 Mm), turn-off (5×5 Mm) and the sub-giant (15×15 Mm) respectively. The darker regions denote downflows, while the lighter regions denote upflows. The granulation patterns suggest that :

- The turn-off star has smaller granules than the Sun. This may be due to the lesser depth of the convection zone.
- The correlation between the velocity at the base of the SAL and in the shallower regions, weakens from the Sun to the sub-giant. This will alter the effective mixing length parameter $\alpha_{\rm eff}$ which is normally assumed to be constant in stellar evolution computations.

Though these only provide a rough idea of apparent trends, we are in the process of computing more quantitative estimates. For example, by computing the velocity power spectrum we can determine the average width of the granules. The value of $\alpha_{\rm eff}$ as a function of position in the $logg-logT_{\rm eff}$ plane can be estimated by either: inserting averages from the 3D simulations into mixing length type expressions; or from two-point correlation functions for velocity, entropy and temperature. We could also use the method described in Ludwig et al. 1999. By matching the mean entropy profiles from a RHD simulation to that of an envelope model, Ludwig et al deduced $\alpha_{\rm eff}$ for a grid of models. All require long time statistical averaging.

7. Conclusions

3D simulations of the upper radiative/convective transition region in the Sun require sophisticated codes which can properly account for varying opacities, partial and full ionisation zones, Coulomb interaction, and heavy element diffusion. This requires a realistic equation of state and non-diffusion approximation radiation in the outer layers.

Such physics is included in the present model. Comparison with previous 3D realistic simulations by SN and computation of p-mode frequencies imply our model is working properly. We intend to apply our model to other stars and as a primary thrust we simulate the turn-off and sub-giant stars. We find that the characteristics of the granules depend on the age of the Sun. It seems the granules are smaller in the turn-off model than in the present Sun.

Acknowledgments. This research is supported in part by NASA grant NAG5-8406 (FJR, PD, SS). YCK is supported by a Department of Astronomy, Yonsei University grant (2001-1-0134). DBG's research is supported in part by a grant from NSERC of Canada. We also would like to acknowledge computer support from the Centre for High Performance Computing at Saint Mary's University in Canada.

References

Alexander, D.R. & Ferguson, J.W. 1994, ApJ, 437, 879

Asplund, M., Ludwig, H.-G., Nordlund, A & Stein, R.F. 2000, A&A. 359, 669

Basu, S. & Antia, H. M. 1997, MNRAS 287,189

Chan, K. L. & Wolff, C. L. 1982, J. Comp. Physics, 47, 109

Chan, K.L. & Sofia, S. 1989, ApJ 336, 1022

Christensen-Dalsgaard & Berthomieu 1991, Solar interior and atmosphere (A92-36201 14-92). Tucson, AZ, University of Arizona Press, 1991, 401-478.

Fryxell et al. 2000, ApJS 131,273

Guenther, D.B. & Demarque, P. 1997, ApJ 484, 937

Guenther, D.B., Demarque, P., Kim, Y.-C. & Pinsonneault, M.H. 1992, ApJ 387, 372

Guenther, D.B. 1994, ApJ 422, 400

Iglesias, C. A., & Rogers, F. J. 1996, ApJ, 464, 943

Kim, Y.-C. & Chan, K.L. 1998, ApJ 496, L121

Kim, Y.-C., Fox, P.A., Sofia, S. & Demarque, P. 1995, ApJ 442, 422

Kim, Y.-C. Fox, P.A., Demarque, P. & Sofia, S. ApJ 461,499

Landau, L.D. & Lifshitz, E.M. 1987, Fluid Mechancis, Course in Theoretical Physics, Volume 6, Pergamon Press.

Li, L.H., Robinson, F.J., Demarque, P., Sofia, S. & Guenther, D.B. 2002, ApJ 567, 1192

Ludwig, H-G., Freytag, B. & Steffen, M. 1999, A&A, 346,111

Lydon, T.J. & Sofia, S. 1995, ApJ 101, 357

Figure 4. Granulation in the Sun (first column), Turn-off (second column) and sub-giant (third column). From top to bottom, each frame depicts a different depth (see text).

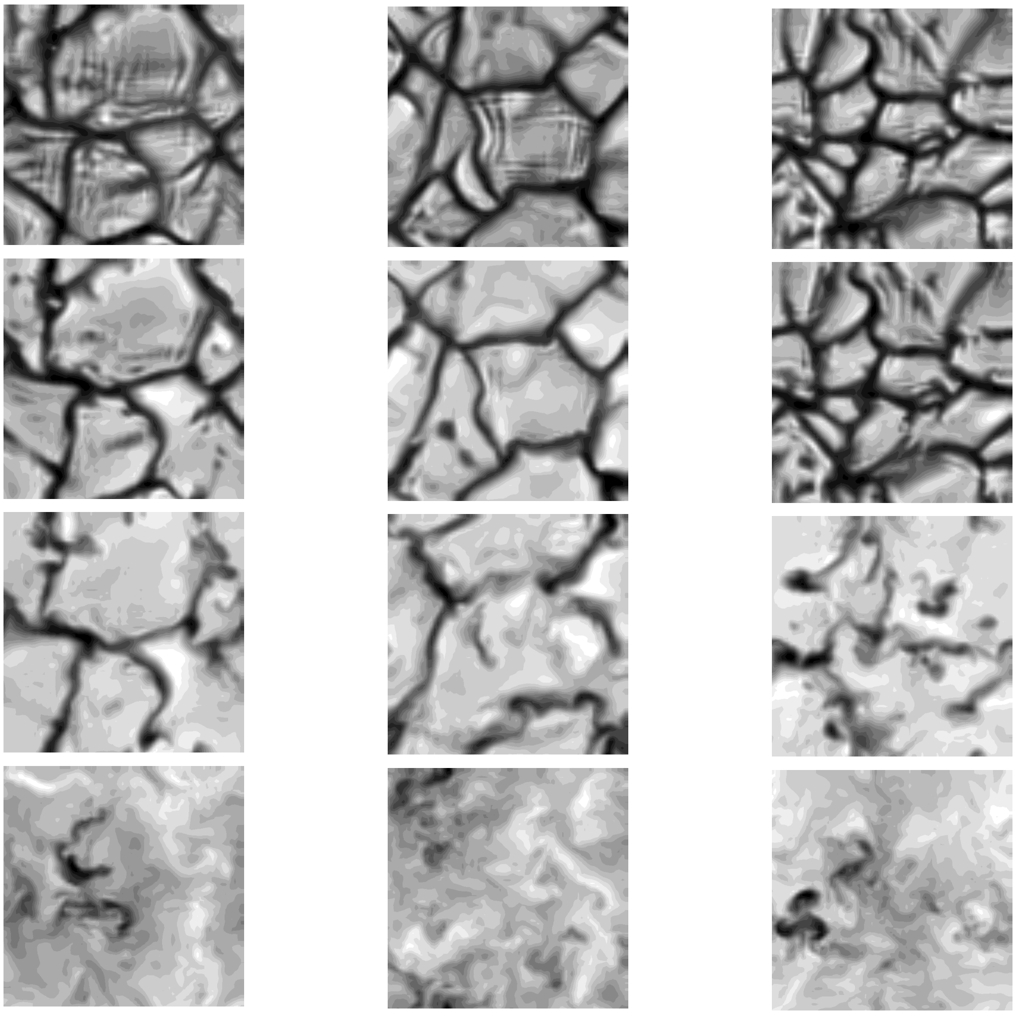

Nordlund, A., 1985, Solar Phys 100, 209

Rosenthal, C.S., Christensen-Dalsgaard, J., Nordlund, Å., Stein, R.F. & Trampedach, R. 1999, A&A, 351, 689

Smagorinsky., J. 1963, Monthly Weather Rev., 91, 99

Stein, R.F. & Nordlund, A 1998, ApJ 499, 914

Stein, R.F. & Nordlund, A 2000 Solar Phys. 192, 91

Unno, W., & Spiegel, E.A. 1966, PASJ, 18, 85

Wedemeyer. S., Freytag, B., Holweger, H., Ludwig, H. & Steffen, M. Astronomische Gesellschaft Abstract Series, Vol. 18., JENAM 2001, abstract P01

8. Appendix : Numerical tests

The characteristics of the models are listed in Table 1. As all the boxes have square cross-section, the aspect ratio is the width divided by the depth. The depths of each simulation, measured from the solar surface, are expressed in Mm, and as the number of pressure scale heights (PSH) over the whole layer. The horizontal grid spacing is the same in the x and y directions.

Table 1. List of Simulations

Model	Width (Mm)	Depth (Mm)	Depth (PSH)	$N_x \times N_y \times N_z$	Δ_x(Km)	Δ_z (Km)
KC/KC2	1.35	0.9	4.4	60^3	26	17.5
A	1.35	2.1	7.2	$59^2 120$	26	17.5
B	1.35	2.8	8.5	$59^2 170$	26	17.5
C	2.7	2.8	8.5	$116^2 170$	26	17.5
D	2.7	2.8	8.5	$58^2 170$	52	17.5
E	5.4	2.8	8.5	$114^2 170$	52	17.5
F	3.75	2.5	8	80^3	47	31.25

The range of simulations was chosen to identify the effect on turbulent pressure $P_{\rm turb}$, turbulent kinetic energy χ and on $\nabla - \nabla_{\rm ad}$ of varying the width and depth of the computational box. They are computed as follows:

1.
$$P_{turb} = \overline{\rho} v_z''^2 / \overline{P}. \tag{16}$$
The turbulent pressure can also be computed as
$$P_{turb} = \overline{\rho (v_z - <v_z>)^2} / \overline{P}, \tag{17}$$
where $< v_z >$ is a horizontal average. Provided the motions were adequately resolved and the integration time was long enough, the two prescriptions for $P_{\rm turb}$ gave the same result.

2.
$$\chi = \frac{1}{2} \frac{\overline{\rho} v''^2}{\overline{P}} = \frac{1}{2} \frac{v''^2}{{c_{\rm s}}^2} \tag{18}$$

where $v''^2 = v_x''^2 + v_y''^2 + v_z''^2$ and c_s is the nondimensional local sound speed.

3.
$$\nabla - \nabla_{\rm ad} = \overline{\frac{\partial \ln T}{\partial \ln P}} - \overline{\nabla_{\rm ad}} \tag{19}$$
where $\nabla_{\rm ad}$ is computed using the OPAL equation of state

8.1. The influence of the impenetrable lower boundary

Starting with KC as an initial model, the lower boundary was moved down in two stages, resulting in models A and B. Simulation A was constructed by adding 3 extra pressure scale heights to the base (see Table 1). The complete layer had a depth of 2.1 Mm (7.2 Pressure scale heights). We first thermally relaxed the lower layer, because with only hydrostatic support (no turbulent pressure), the overlying layer collapsed, and the simulation crashed. Also, when joining the two layers, the turbulent viscosity was temporarily increased. This smoothed out the fluctuations that were produced, by suddenly removing the lower boundary. Model B was made by adding a hydrostatic layer computed using MLT, to model A. This increased the depth from 2.1 Mm to 2.8 Mm. As the turbulent pressure near the bottom of model A was small (about 1 % of the gas pressure), in this case we did not need to relax the hydrostatic lower layer separately.

Speeding up the flow To demonstrate the effect of the lower boundary on the turbulent flow, we computed the ratio of horizontal kinetic energy to the gas pressure. This is equivalent to the horizontal turbulent Mach number squared, i.e..
$$\chi_{\rm horiz} = \frac{1}{2}\overline{\rho}(v_x''^2 + v_y''^2)/\overline{P} = \frac{1}{2}(v_x''^2 + v_y''^2)/{c_s}^2 \tag{20}$$
Figure 6 (a) shows $\chi_{\rm horiz}$ for models KC, A and B. In the shallow model (KC), the magnitude of $\chi_{\rm horiz}$ shoots up at the base. The net effect when the fast downflows strike the lower boundary is to speed up the overall flow. This increases the total turbulent kinetic energy throughout the box (Figure 6 (b)).

The upturn at the base is clearly reduced as the boundary is moved deeper. It is almost entirely eliminated in model B. Note, the problem is much less severe at the top boundary because the underlying region is sub-adiabatic (the radiative zone). The vertical velocity is already small when the flow hits the top boundary.

Effect on superadiabaticity The faster flow produces more efficient convection and a reduction of $|\nabla - \nabla_{\rm ad}|_{\rm max}$. The run of $\nabla - \nabla_{\rm ad}$ for MLT, and models KC, and B are shown in the figure 5. The shallow layer has a broader and lower SAL peak than MLT, while the deeper box has a higher peak. The higher peak is the correct one.

8.2. Domain width

Models B, D and E have widths of 1.35, 2.7 and 5.4 Mm. To judge the effect of width on simulations without changing the grid spacing, we should compare B

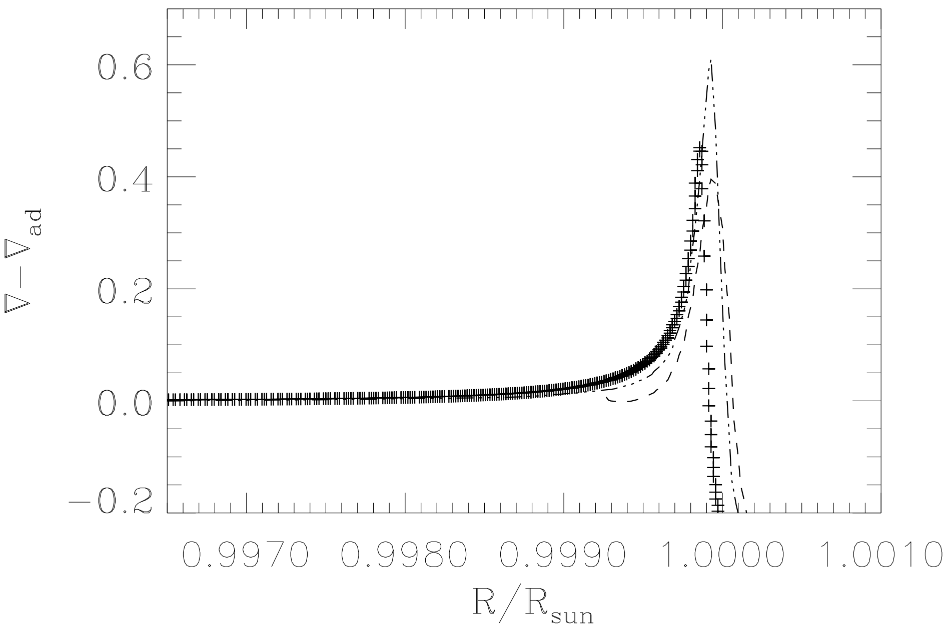

Figure 5. Superadiabacity as a function of domain depth. The 3D models KC2 and C are denoted by dashed and triple-dot-dashed lines, while the mixing length model is denoted by pluses. If the lower boundary is too close to the SAL (as it is in KC2) then the flow can be speeded up and the height of the SAL, compared to MLT, is reduced.

to C and D to E. Increasing the width had a negligible effect on either $P_{\rm turb}$ or $\nabla - \nabla_{\rm ad}$.

The variation of kinetic energy χ with domain width is more interesting (Figure 7). When the width is increased from 1.35 to 2.7 Mm the kinetic energy near the top increases. However, when it is increased from 2.7 to 5.4 Mm there is no change in χ. To resolve χ for solar granules, 2.7 Mm seems to be a sufficient width.

In the SAL the granules contain most of the kinetic energy and while larger cells are introduced by an increase from 1.35 to 2.7, none are by the further increase to 5.4 Mm. This can be seen from horizontal contour plots of vertical velocity for models of different widths (figure 8). The uppermost frame shows that not even a single granule can fit in the box when the width is 1.35 Mm, while about 2 of the largest cells fit easily in to the box in the second frame. As the width is further increased, more cells are seen but their sizes are about the same. In the final frame about 9 or 10 larger cells can fit in to the box. Due to computational restrictions the last figure is computed on a coarser mesh than the previous three frames. While this has an effect on the fine scales, it has little effect the size of the larger granules.

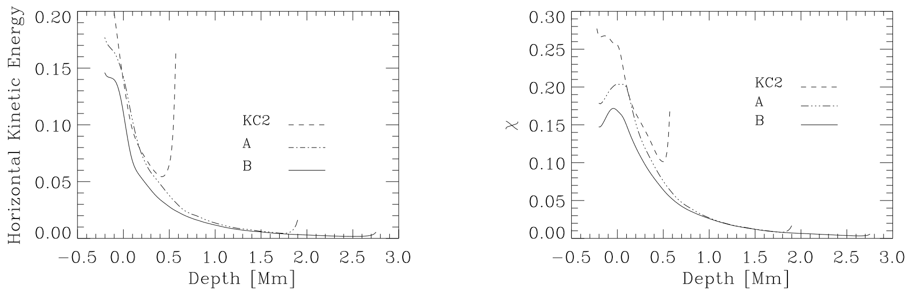

Figure 6. Horizontal turbulent kinetic energy (figure (a)) and total turbulent kinetic energy (figure (b)), both as a function of depth

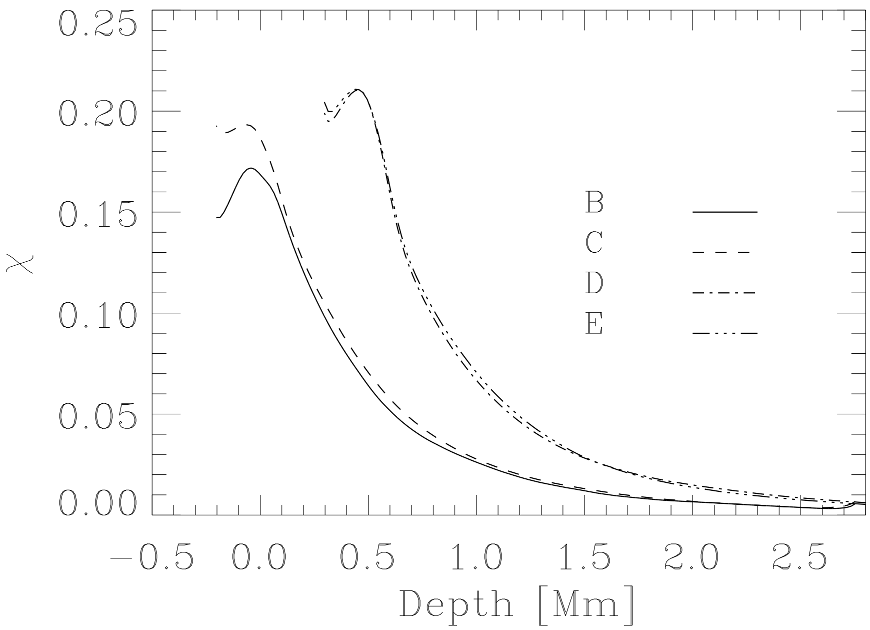

Figure 7. Total turbulent kinetic energy as a function of domain width.

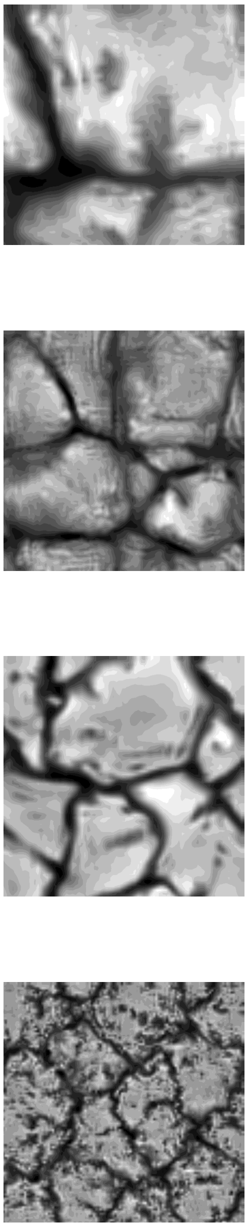

Figure 8. Granulation at the peak of the SAL for different domain widths. From top to bottom of the figure, shows contours of vertical velocity for widths of 1.35, 2.7, 3.75 and 5.4 (low horizontal resolution). At least 2 cells are needed in to get the kinetic energy correct.

8.3. Numerical resolution

While the main point of these tests is to show that the domain size has a significant effect on granular convection, we have also partially addressed the effect of changing the horizontal and vertical grid spacing. Models C and D produced very similar P_{turb} and $\nabla - \nabla_{\mathrm{ad}}$ (not shown), while χ differed only above the SAL. This we believe reflects the sensitivity of the horizontal part of the kinetic energy in the radiation layer. Strong horizontal velocities have long been know to exist above the surface (e.g. Kim et al 1996).

In Asplund et al. it was found that the velocities had a much stronger dependence on horizontal resolution than we found in our computations. We are not sure why this is, but speculate that it is because of the different sub-grid models employed. With a value of $C_\mu = 0.04$ and setting C as small as possible (see section 2.3.) we might have a smaller viscous dissipation length $C_\mu \Delta$, than in the SN model. Presumably if SN increases the number of grid points then at one stage their dissipation length would match ours. This might explain why we find less sensitivity to resolution than in Asplund et al.

Model F which has coarser vertical resolution than the other models, has nearly the same P_{turb}, χ and $\nabla - \nabla_{\mathrm{ad}}$ as the other deep models.